NeuroImage 223 (2020) 117318

Contents lists available at ScienceDirect

NeuroImage

journal homepage: www.elsevier.com/locate/neuroimage

Diffusion functional MRI reveals global brain network functional abnormalities driven by targeted local activity in a neuropsychiatric disease mouse model

Yoshifumi Abe[a,*], Norio Takata[a], Yuki Sakai[b,c], Hiro Taiyo Hamada[d], Yuichi Hiraoka[e], Tomomi Aida[e], Kohichi Tanaka[e], Denis Le Bihan[f,g], Kenji Doya[d], Kenji F Tanaka[a]

[a] Departemnt of Neuropsychiatry, Keio University School of Medicine, 35 Shinanomachi, Shinjuku, Tokyo, Japan
[b] ATR Brain Information Communication Research Laboratory Group, Kyoto, Japan
[c] Department of Psychiatry, Graduate School of Medical Science, Kyoto Prefectural University of Medicine, Kyoto, Japan
[d] Neural Computation Unit, Okinawa Institute of Science and Technology, Okinawa, Japan
[e] Department of Molecular Neuroscience, Medical Research Institute, Tokyo Medical and Dental University, 1-5-45 Yushima, Bunkyo, Tokyo, Japan
[f] NeuroSpin, Commissariat à l'énergie atomique et aux énergies alternatives, Gif-sur-Yvette, France
[g] Department of System Neuroscience, National Institutes for Physiological Sciences, Okazaki, Japan

ARTICLE INFO

Keywords:
Diffusion function MRI
Ignition-driven mean integration analysis
Functional connectivity
Apparent diffusion coefficient
Blood oxygenation-level dependent signal

ABSTRACT

Diffusion functional magnetic resonance imaging (DfMRI) has been proposed as an alternative functional imaging method to detect brain activity without confounding hemodynamic effects. Here, taking advantage of this DfMRI feature, we investigated abnormalities of dynamic brain function in a neuropsychiatric disease mouse model (glial glutamate transporter-knockdown mice with obsessive–compulsive disorder [OCD]-related behavior). Our DfMRI approaches consisted of three analyses: resting state brain activity, functional connectivity, and propagation of neural information. We detected hyperactivation and biased connectivity across the cortico-striatal-thalamic circuitry, which is consistent with known blood oxygen-level dependent (BOLD)-fMRI patterns in OCD patients. In addition, we performed ignition-driven mean integration (IDMI) analysis, which combined activity and connectivity analyses, to evaluate neural propagation initiated from brain activation. This analysis revealed an unbalanced distribution of neural propagation initiated from intrinsic local activation to the global network, while these were not detected by the conventional method with BOLD-fMRI. This abnormal function detected by DfMRI was associated with OCD-related behavior. Together, our comprehensive DfMRI approaches can successfully provide information on dynamic brain function in normal and diseased brains.

1. Introduction

Repetitive behaviors are one of the behavioral hallmarks of neuropsychiatric disorders including obsessive-compulsive disorder (OCD), autism spectrum disorders (ASD), and Tourette's syndrome (TS)(Ade et al., 2016; Bronfeld and Bar-Gad, 2013; Ellegood et al., 2013; Stoodley et al., 2017). Resting state functional magnetic resonance imaging (fMRI) has been used to examine functional connectivity (FC) alterations in patients with these disorders (Cerliani et al., 2015; Hou et al., 2014; Jung et al., 2017; Neuner et al., 2014; Rane et al., 2015). In particular, abnormal FC alterations in the cortico-striatal-thalamo (CST) circuitry were found in OCD patients (Hou et al., 2014; Jung et al., 2017). In addition, OCD patients exhibited neural hyperactivity in the orbitofrontal-striatal network (Hou et al., 2014; Yang et al., 2019). An animal study also reported that optogenetic-induced excitation of orbitofrontal (ORB) neuron terminals in the ventral striatum of mice increased grooming behavior, a known repetitive behavior (Ahmari et al., 2013), suggesting that neural hyperactivation in the ORB is related to the underlying mechanism that generates repetitive behavior. However, the mechanism by which hyperactivation impacts dynamic brain function remains controversial.

All of these studies were performed using blood oxygenation-level dependent (BOLD)-fMRI, a powerful tool for investigating whole brain functional connectivity as well as brain activity, based on the neurovascular coupling hypothesis. However, BOLD-fMRI may fail when neurovascular coupling is impaired (e.g. cerebrovascular disease, astrocytic dysfunction, or drug intake such as anesthetized conditions) (Abe et al., 2017a; Shih et al., 2009; Veldsman et al., 2015). For example, patients with Alzheimer's disease show impaired vascular responses (Kisler et al., 2017; Montagne et al., 2016). Similarly, animal studies conducted under

* Corresponding author.
E-mail address: yoshifumi.abe@keio.jp (Y. Abe).

https://doi.org/10.1016/j.neuroimage.2020.117318
Received 18 March 2020; Received in revised form 23 August 2020; Accepted 25 August 2020
Available online 1 September 2020

anesthetized conditions exhibit large variations in hemodynamic patterns depending on the anesthetic drugs used (Sforazzini et al., 2014; Zerbi et al., 2015). Thus, BOLD-fMRI under these conditions may lead to false-positive or false-negative results when investigating brain networks and activity.

In contrast, diffusion fMRI (DfMRI) is an alternative approach to BOLD-fMRI which is not impaired by those confounds, and more directly reflects neural activity than BOLD-fMRI regardless of hemodynamic status (Abe et al., 2017a; Le Bihan et al., 2006; Tsurugizawa et al., 2013). While controversial when first introduced (Bai et al., 2016; Jin and Kim, 2008; Miller et al., 2007), the nonvascular nature of the DfMRI signal has since been established, although its exact mechanism (activation-induced neuronal swelling but not astrocytic swelling, as suggested from pharmacological DfMRI studies (Abe et al., 2017a; Komaki et al., 2020) and single neuron microscopic DfMRI (Abe et al., 2017b)) remains to be validated. In those previous studies, two types of DfMRI signals were identified as good markers of neural activity: diffusion-weighted signals obtained with b=1800 s/mm^2 (S_{b1800}) and the water apparent diffusion coefficients (ADCs) (Abe et al., 2017a; Cotero et al., 2019; Tsurugizawa et al., 2013; Zhong et al., 1997). In addition, DfMRI also has the potential to allow for FC analysis without interference from hemodynamics. While, thus far, there have been no reports of FC analysis based on DfMRI signals, a previous DfMRI study using pharmacological modulators of cellular swelling suggested that DfMRI may actually track activity across brain networks (Abe et al., 2017a). Another group has also shown connectivity of the thalamocortical pathway by coherence analysis of DfMRI time-series data (Nunes et al., 2019).

In this study, we investigated abnormalities of dynamic brain function in a neuropsychiatric mouse model (glial glutamate transporter [GLT1]-knockdown mice, GLT1-KD mice) exhibiting OCD-related behavior (Aida et al., 2015), by leveraging the advantages of DfMRI. Our DfMRI approaches analyzed three brain dynamic processes: resting state brain activity, FC, and propagation of neural information (See Fig. 1A). This approach confirmed the hyperactivation and abnormal connectivity of the CST circuitry, as suggested from previous findings in OCD patients. Furthermore, we revealed abnormal propagation of local activity to the global network in GLT1-KD mice.

2. Materials and methods

2.1. Animals

We employed astrocytic glutamate transporter knockdown (GLT1-KD) mice (Aida et al., 2015). The GLT1-KD mice (GLAST$^{CreERT2/+}$; GLT1$^{flox/flox}$, n=14) were generated by mixing homozygous GLT1$^{flox/flox}$ with heterozygous inducible Cre recombinase (CreERT2) in an astrocyte-specific GLAST locus (GLAST$^{CreERT2/+}$) (Fig. 1B). The GLT1-KD mice were crossed with the 129Sv and C57BL/6 strains. GLT1-KD mice showed knockdown not only of astrocytic GLT1, but also of astrocytic GLAST. GLAST$^{+/+}$; GLT1$^{flox/flox}$ mice were used as controls (ctl, n=14). Both groups were injected intraperitoneally with 100 mg/kg tamoxifen (TAM) at postnatal days 17-21 for five consecutive days to induce the deficit in astrocytic glutamate transporters.

All animal experiments were approved by the Okinawa Institute of Science and Technology Graduate University (approval number: 2014-091). All animals were housed in temperature- and humidity- controlled rooms on a 12 h light/dark cycle (lights on at 8:00 AM).

2.2. Behavioral monitoring

Prior to the MR imaging studies, we recorded the repetitive tic-like behavior (Aida et al., 2015). Mice were put into a cylindrical, acrylic chamber (diameter: 12 cm, height: 22 cm) and their behavior was recorded for 10 min with a video camera. Tic-like movements were counted manually and quantified as the total number of tics observed in an individual mouse during the 10-min recording data. Observers were blinded to the genotype status. The behavior was defined as any brief isolated head and/or body jerk or shake. Using the logged times of each tic in the recoding data, the tics were subsequently replayed in slow motion to categorize their type of movement. The possible types of tic movement included shaking of the head or whole body (rotational vector); and jerking of the head, body or part of the body in one or more directions.

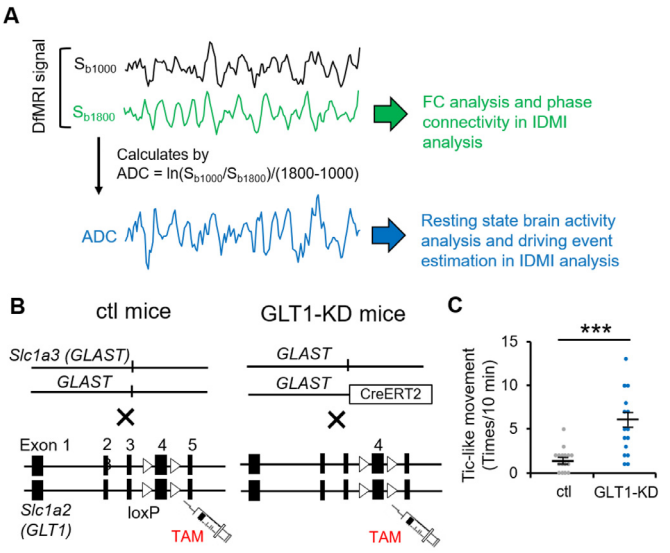

Fig. 1. A schematic diagram of the DfMRI analysis in a GLT1-KD mouse. (A) A schematic diagram of the DfMRI analysis. Two types of time series signals of DfMRI with b=1000 and 1800 mm ^{2}/s (S_{b1000} and S_{b1800}, respectively) were obtained from GLT1-KD and control mice in resting state and awake conditions. The time series data for the ADC were computed with the time series data from S_{b1000} and S_{b1800}. The ADC was used to investigate resting state brain activity and to define the driving events ignited by neural excitation in the IDMI analysis. The S_{b1800} was used to analyze the FC and to calculate the phase connectivity for the IDMI analysis. (B) GLT1-KD mice were crossed with GLAST$^{CreERT2/+}$ and GLT $^{flox/flox}$ and the GLT1 deficit was induced by tamoxifen (TAM) injection. Control (ctl) mice were crossed with GLAST$^{+/+}$ and GLT $^{flox/flox}$. (C) Tic-like behavior, which was counted over 10 minutes, was increased in GLT1-KD mice (n=14 in ctl and n=14 in GLT1-KD mice, two-sided t-test, t(26)=4.11, p=3.52 × 10^{-4}). *** p<0.001. The horizontal lines represent the mean and the vertical lines represent the standard error (s.e.m).

2.3. Immunohistochemistry

After MRI, mice were deeply anesthetized with a ketamine-xylazine mixture and transcardially perfused with 10 ml of 0.1 M phosphate-buffer solution (PBS, pH 7.4) containing 4% (w/v) paraformaldehyde (PFA). The brains were post-fixed overnight with 4% PFA for 1 day. The fixed brains were cryoprotected in 20% sucrose/phosphate buffered saline (PBS) for 1 day frozen, and coronal sections were cut at a thickness of 25 μm on a cryostat. Serial brain sections were used for the subsequent immunohistochemistry. The serial sections were incubated with anti-GLT1 rabbit monoclonal antibody (1:1000 dilution, Frontier Institute Co., Ltd, Hokkaido, Japan) overnight at room temperature. The sections were then incubated with secondary antibodies conjugated to Alexa Fluor 555 (1:1000; Invitrogen, Grand Island, NY, USA) for 2 hours at RT. Images of the sections were captured using an inverted light microscope (BZ-X710, Keyence, Osaka, Japan). ImageJ software (http://rsb.info.nih.gov/ij/) was used for image analysis to calculate the percentage of the area expressing GLT1. All images were binarized. The positive area of GLT1 expression was defined by a threshold to distinguish GLT1 positive versus negative areas. Then, the percentage of the GLT1 expression area was calculated. We estimated the ratio of GLT1

expression as ($GLT1_{KD}$-$GLT1_{ctl}$)/$GLT1_{ctl}$ × 100, where $GLT1_{KD}$ is the mean percentage area of GLT1-positive cells in GLT1-KD mice.

2.4. Surgery and acclimation for awake MRI

The detailed method has been described in previous publications (Takata et al., 2018; Yoshida et al., 2016). Briefly, an acclimation bar was surgically implanted on the mouse skull at 8 weeks of age. Mice were injected intraperitoneally with an anesthetic mixture of 0.3 mg/kg medetomidine, 4 mg/kg midazolam, and 5 mg/kg butorphanol, and fixed to a stereotaxic apparatus (SM-15, Narishige Scientific Instrument, Tokyo, Japan). The skull surface was exposed. The periosteum and blood were removed thoroughly. A custom-made acrylic head bar (3 × 3 × 27 mm^3) was mounted along the sagittal suture of the exposed skull using dental cement (Super-Bond C&B, Sun Medical, Shiga, Japan) in awake mice. After surgery, the mice were fed a high-energy diet (CMF sprout; Oriental Yeast Co., Kyoto, Japan) afterward instead of normal chow, to facilitate recovery of bodyweight. After the mice recovered their weight, they were acclimated to a mock fMRI environment for 2 hours/day for 10 days before performing the experimental fMRI in awake mice. For mice during the habituation, the head-bars were clamped to a specific holder that was then secured tightly on a mock animal bed through the base. The trunk of the mouse outside the mock bed was covered gently with a sheet of a paper to relieve the animal. A pad was laid under the mouse for urine absorption. Awake animals were restrained in this mock fMRI environment while a recording was played of scanner noises at 100 dB that was comparable to those in the actual fMRI experiments. This was performed within a soundproof box that imitated the dark environment of the actual fMRI measurements.

2.5. MRI acquisition

The MRI was conducted under awake conditions on a 11.7T scanner equipped with a cryoprobe and a gradient system, which allowed a maximum gradient strength of 1000 mT/m (BioSpec, Bruker, Ettlingen, Germany). Respiration rate and rectal temperature (37°C) were monitored during scanning. Body temperature was maintained at 37°C using an MR-compatible, feedback-controlled water heating system. Initially, we determined the position of the brain between +2.8 and -6 mm from the bregma, using anatomical images acquired along three orthogonal directions.

The detailed DfMRI protocol was described in a previous paper (Abe et al., 2017a; Tsurugizawa et al., 2013). Resting state DfMRI (no stimulation) was acquired with the following parameters: diffusion-sensitized double spine echo (SE)-echo planner imaging (EPI) sequence; TR/TE=2000/37 ms, segments=1, FOV=16 × 16 mm^2, matrix=80 × 80, slice thickness=0.8 mm, slice gap=0.05 mm, slice number=10, repetition number=150, scan time=10 min, and b-values=1000 and 1800 mm^2/s along 1 directions; [X=1,Y=1,Z=1]. Resting state BOLD-fMRI was acquired with the following parameters: gradient echo (GE)-EPI sequence; repetition time (TR)/echo time (TE)=2000/13 ms, segments=1, FOV=16 × 16 mm^2, matrix=80 × 80, slice thickness=0.4 mm, slice gap=0.05 mm, slice number=20, repetition number=300, scan time=10 min. After the acquisition of DfMRI and BOLD images, structural (anatomical) images for spatial normalization were obtained using a 3D-multislice rapid acquisition with relaxation enhancement (RARE) sequence in the same brain locations and with the following parameters: TR/TE=1800/32 ms, FOV=15 × 15 × 12.5 mm^3, matrix=256 × 256 × 32, resolution=0.059 × 0.059 × 390 mm^3, average=1, scan time=17 min.

2.6. Preprocessing of BOLD-fMRI and DfMRI images

Preprocessing and statistics were performed using SPM12 (Welcome Trust Centre for Neuroimaging, London, UK) and in-house software written in MATLAB (Abe et al., 2017a). Initial image preprocessing was performed individually for each animal. The 3D-RARE reference images were co-registered and spatially normalized to a standardized structural brain template for mice (Hikishima et al., 2017). The time-series images (DfMRI obtained with b1000 and b1800 mm^2/s, and BOLD-fMRI) were realigned to correct for residual head motion, corrected for slice timing, and co-registered to the reference structural images. Then, all images where spatially normalized and co-registered to the standardized brain structure template using the normalized parameters of the structural image. Finally, these images were resliced to a resolution of 0.2 × 0.2 × 0.2 mm^3 and smoothed with a full width at a half maximum (FWHM) Gaussian kernel of 0.6 mm. For the BOLD-fMRI, we decreased the sampling rate of the time-series data from 0.5 Hz (equal to TR=2s) to 0.25 Hz (equal to TR=4s) to allow for the comparison between the DfMRI and BOLD-fMRI. Then, the pre-processing was performed using this down sampled BOLD-fMRI data in the same way as the DfMRI.

To provide some indication of the overall signal level in our image data, the signal-noise ratio (SNR) was estimated for the whole brain of each control animal and for each of the first 5 raw time course images before preprocessing. The SNRs were calculated by dividing the signal of the whole brain by the signal outside of the brain for each animal. The averaged SNR values (mean±s.e.m, n=14) were 10.57±0.36 for S_{b1000}, 7.07±0.15 for S_{b1800}, and 17.82±0.61 for BOLD-fMRI (Figure S1B).

2.7. ADC analysis of resting state neural activity

The ADCs were calculated from the preprocessed time series images of the diffusion weighted signal acquired at b=1000 and 1800 mm^2/s (S_{b1000}, S_{b1800}) for each time point as ADC=ln(S_{b1000}/S_{b1800})/800 to remove any residual T2/T2* (BOLD) effects (Abe et al., 2017a).

To evaluate the local neural activity between GLT1-KD and ctl mice, we performed a voxel-based comparison of the baseline magnitude of the ADC time-series data. The time-series images of the ADCs for each animal were averaged and pooled for the group analysis. Then, a two-sample t-test was performed with family wise error (FWE) correction $p<0.05$. The statistical overlay maps were created using MRIcron (available at: http://www.cabiatl.com/mricro/mricron/install.html) to show regional ADC changes between ctl and GLT1-KD mice. For the region of interest (ROI)-based comparisons of the ADC time course data, the ADCs were extracted for each ROI, which included 59 bilateral brain loci defined in our flexible annotation atlas (FAA) of the mouse brain (See Fig. S1A and Table S1) (Takata et al., 2020). The FAA is based on the Allen Mouse Brain Atlas, which can be reconstructed with a text-based information and Python codes (https://github.com/ntakata/flexible-annotation-atlas/tree/master/FAAs/others/FAAocd). The ADCs were first averaged at each time point over all voxels for each ROI in individual animals, then averaged for each ROI over all animals. When we compared the magnitude of the BOLD signal, we performed the statistical analysis in the same manner as described above. A power spectrum was calculated with the detrended ADC time series data using the MATLAB code “mtspecgramc.m” in the chronux toolbox (available at: http://chronux.org/). The frequency analysis of the ADC driving events is described in the methods section for the IDMI analysis.

2.8. Functional connectivity (FC) analysis

The pre-processed time series data from S_{b1800} were used for the FC analysis with the functional connectivity toolbox (CONN, available at: https://www.nitrc.org/projects/conn) and in-house software written in MATLAB. The time-series data were detrended and temporally filtered with 0.01-0.1 Hz. The global mean signal was regressed out from the preprocessed time series data in order to reduce non-neural signal correlations. A seed-based FC analysis was performed using the pre-processed time-series data. The ROIs from 59 bilateral brain loci were defined in the FAA. Pair-wise Pearson’s correlation coefficients between the time course of a predetermined ROI and all other ROIs were estimated after

de-noising and de-spiking and were transformed into Fisher's z-scores. Regions of white matter and cerebrospinal fluid were excluded, then a 59 × 59 connectivity matrix was generated. When we compared the FC connectivity matrix between ctl and GLT1-KD mice, a Student's t-test with false discovery rate (FDR) correction $p<0.05$ was performed. Then, the FC values with significant differences were estimated.

2.9. Ignition-driven mean integration (IDMI) analysis

The methods for the IDMI analysis were based on a previous publication (Deco et al., 2017). IDMI is a global measure of dynamic complexity that can be obtained in four steps: 1) the detection of neural activation for a brain region as an intrinsic driving event using a threshold method for the ADC or BOLD-fMRI time series, 2) the calculation of the pair-wise phase synchronization at time t between brain regions j and k [$P_{jk}(t)$], 3) the construction of a binarized phase lock matrix by time-averaging $P_{ij}(t)$, and 4) obtaining the IDMI as the path-length of the largest subcomponent of the binarized phase lock matrix.

An intrinsic driving event for a particular brain region was defined as an event of neural excitation under the resting state condition. An ADC reduction and a BOLD increase was considered to be neural excitation, respectively (Abe et al., 2017a; Zhong et al., 1997). Particularly, the time-series data from the ADC and BOLD images were transformed to z-score time-series data. An ADC intrinsic driving event was defined as an event where the z-score time series exceeded the threshold of one standard deviation from the time series, and the time series of the ADC decreased (See the blue lines in Fig. 5A) (Tagliazucchi et al., 2012). In contrast, a BOLD intrinsic driving event was defined as an event where the z-score time series exceeded the threshold of one standard deviation of the time series, and the time series of the BOLD signal increased. Intrinsic driving events were estimated in the 59 bilateral brain loci defined from the FAA. Of note, the ADC and BOLD-fMRI signals are absolute and relative measures of neural activity, respectively.

To calculate the pair-wise phase synchronization (phase connectivity), we first filtered the S_{b1800} and BOLD-fMRI time series in the range of 0.05-0.08 Hz, and extracted the phases using a Hilbert transform. The same range filter was applied for the BOLD-fMRI. Then, the pair-wise phase synchronization between the regions j and k at time t was calculated as:

$$P_{jk}(t) = e^{-3\left|\varphi_j(t)-\varphi_k(t)\right|} \quad (1)$$

where $\varphi_j(t)$ is the extracted phase of brain area j at time t.

A phase lock matrix was calculated using $P_{ik}(t)$. More specifically, $P_{jk}(t)$ was first averaged from an intrinsic driving event for a time window of six TRs from the DfMRI or BOLD-fMRI time series, then averaged for every intrinsic ignition event. The time window (six TRs) to calculate a phase lock matrix was determined as the time necessary for the DfMRI signal to return to the basal level after an intrinsic ignition event (Figure S4A). The time-averaged $P_{ik}(t)$ was used as an element of the phase lock matrix. This time window was applied to the BOLD-fMRI to maintain a justifiable comparison of the IDMI values between the DfMRI and BOLD-fMRI.

The phase lock matrix can be binarized with a threshold θ between 0 and 1 (0 if $|P_{jk}| < \theta$, 1 otherwise), resulting in a symmetric, binarized adjacency matrix. By regarding the adjacency matrix as an undirected graph, the integration value can be computed as a ratio of the path length of the largest subcomponent of the graph to that of the whole graph. These calculations were performed using the MATLAB code "get_components.m" in the Brain Connectivity Toolbox (https://sites.google.com/site/bctnet/). Finally, the IDMI value was computed as the area under the curve (AUC) for all integration values at all threshold values (0 to 1). The IDMI values of the S_{b1000} and ADC for Figure S6 were calculated in the same manner.

To assess the validity of the IDMI analysis, we tested whether the IDMI values obtained from the measured data were significantly higher than those obtained with shuffled, randomized data. To achieve this, the IDMI value was calculated after random permutation of the phase time series from the S_{b1800} or BOLD-fMRI. We repeated this procedure 50 times and compared the average IDMI values obtained with the measured versus permutated data.

To compare the frequency of the ADC-driving events, we counted all driving events for all brain loci. To compare the synchronization of the event frequency, the PSTHs of the ADC-driving events were calculated. The brain regions used to compute the driving events were limited to the CST circuitry. The number of events were counted in all brain regions, then averaged over the regions and every TR time (4 seconds). To verify the effect of head motion during the scan, we calculated the framewise displacement (FD) from six parameters of head motion, which were estimated during the realignment process (Power et al., 2012). IDMI values did not show a significant correlation with head motion (Figure S5), indicating that head motion during the acquisition of DfMRI did not affect the IDMI values.

2.10. Statistics

Statistical processing was performed using MATLAB (MathWorks, MA, USA) and Excel software (Microsoft, USA). Familywise error (FWE) correction was conducted for the voxel-based analysis of ADC-DfMRI. Bonferroni corrections or false discovery rate (FDR) corrections were applied to correct p-values for multiple comparisons. Values are shown as the mean±standard error of the mean (SEM) or as scatter diagrams with crossbars showing the average values.

3. Results

3.1. GLT1-KD mice exhibit tic-like behavior

Repetitive tic-like behavior in astrocytic GLT1-KD and control (ctl) mice was compared (Fig. 1B). GLT1-KD mice showed a significant increase in tic-like behavior, compared with ctl mice (Fig. 1C), consistent with our previous study (Aida et al., 2015). In addition, we investigated the knockdown ratio of GLT1 by immunohistochemistry. In GLT1-KD mice, GLT1-positive neuropils in astrocytic cells were sparse (Figure S2A). The percentage area of GLT1-positive cells was significantly decreased in GLT1-KD mice (Figure S2B, C).

3.2. ADC-DfMRI reveals hyperactive resting state activity in the CST circuitry of GLT1-KD mice

The ADC values obtained by DfMRI were used as a quantitative marker of resting state activity without hemodynamic confounds. Previous studies have shown that the magnitude of the ADC baseline under resting state conditions reflects resting state activity (Abe et al., 2017a; Abe et al., 2017b). In contrast, the baseline BOLD-fMRI signals are only relative and can be contaminated by hemodynamic confounding effects (Abe et al., 2017a). Indeed, the magnitude of the BOLD signal was decreased throughout the entire brain of the GLT1-KD compared to ctl mice (Figure S3A), suggesting that the BOLD signal is not suitable to evaluate resting state activity, because it is a relative measurement and highly dependent upon vascular effects. In contrast, the average ADC baseline ($ADC_{baseline}$) only differed between ctl and GLT1-KD mice in selected areas (Fig. 2B). Compared to ctl, the voxel-based analysis of the magnitude of the $ADC_{baseline}$ value in the GLT1-KD mice showed significant reductions in the MO, SS, PL, ILA, ORB, AI, CP, ACB, PALv, MED, and the hippocampus, while increases were observed in the thalamic regions (See abbreviation list in Table S1). The ROI-based analysis showed significant reductions in the $ADC_{baseline}$ in the MO, SS, PL, IL, ORB, AI, ACB, PALd, PALv, and MED regions in the GLT1-KD mice (Fig. 2C). Based on a previous report, this decrease in the ADC may be interpreted as an increase in resting state activity (Abe et al., 2017a).

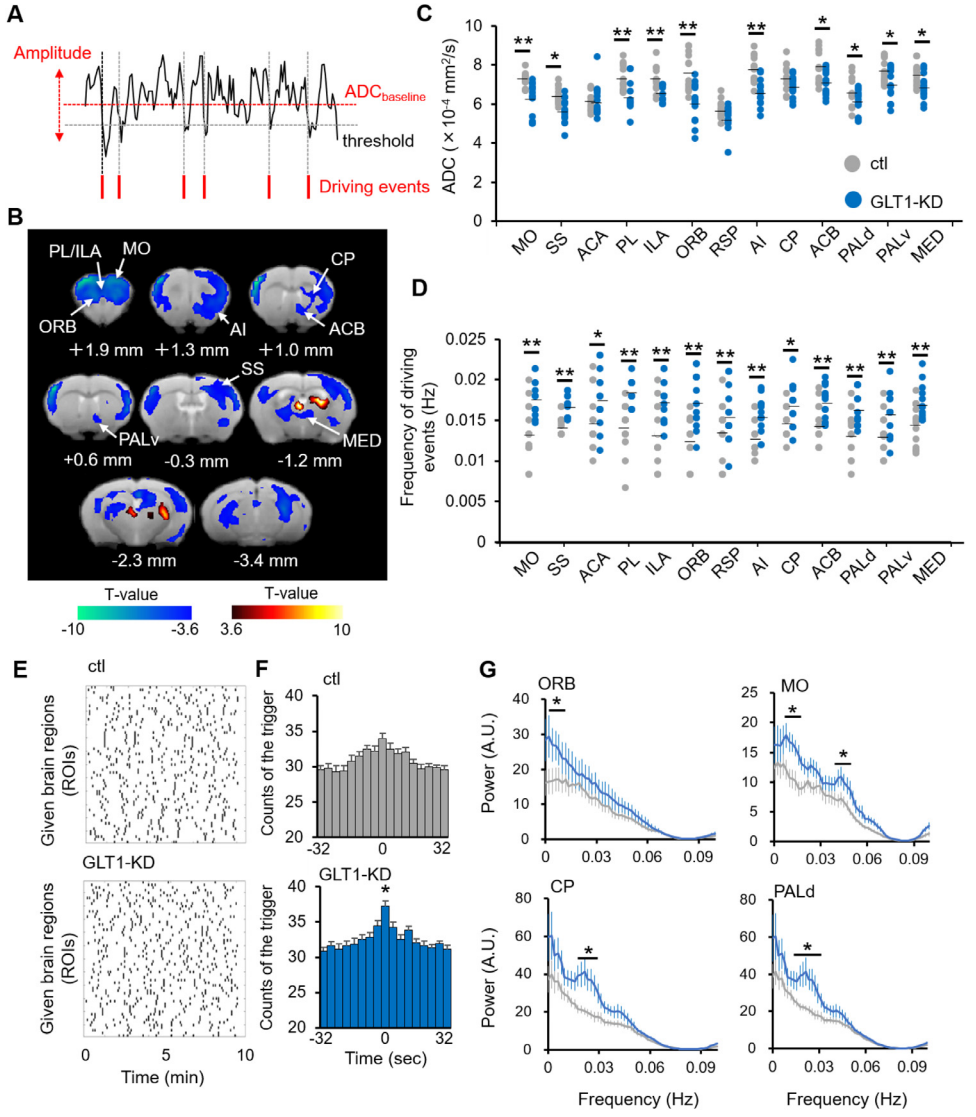

Fig. 2. ADC-DfMRI detected hyperexcitation of CST circuitry in GLT1-KD mice. (A) Three analyses of the ADC time-series data: 1) magnitude of the ADC baseline, 2) frequency of the ADC driving events, and 3) the ADC amplitude. (B) Voxel-based comparison of the ADC map between GLT1-KD (n=14) and ctl mice (n=14). The blue areas represent significant decreases in ADC coupled with an increase in resting state activity, while the red/yellow areas represent the opposite (FWE corrected p<0.05). The numbers below the maps represent distance from the bregma. (C) The magnitude of the ADC baseline was compared in the MO, SS, ACA, PL, ILA, ORB, RSP, AI, CP, ACB, PALd, PALv, and MED between GLT1-KD and ctl mice. Horizontal lines represent the mean. (D) The frequency of the ADC driving events was compared between GLT1-KD and ctl mice. (E) Representative plots of the ADC driving events for all times and 59 given brain regions in ctl (upper) and GLT1-KD (lower) mice. Each single vertical bar represents an ADC driving event. (F) The PSTHs of the ADC driving events in the ctl (upper) and GLT1-KD (lower) mice (two-way repeated-measures ANOVA with Bonferroni post hoc test, main effect of genotype $F_{1,442}$=54.39, p=8.18 × 10^{-13}, main effect of time $F_{16,442}$=10.22, p=3.99 × 10^{-22}, interaction effect $F_{16,442}$=0.50, p=0.95; post hoc test: ctl vs. GLT1-KD in time 0 sec p=0.047. Bars represent the mean and lines represent the standard error (s.e.m.). The PSTHs were averaged across the brain regions of the CST circuitry. (G) The averaged power spectra of the ADC time course from the ORB, MO, CP, and PALd. Polygonal lines represent the mean and vertical lines represent the s.e.m.. * p<0.05, ** p<0.01 (Bonferroni-corrected p-value of the two-sided t-test: ctl vs. GLT1-KD).

In general, it is thought that the ADC values reflect changes in the underlying static tissue microstructure (Le Bihan, 2007; Le Bihan and Iima, 2015). Here, to demonstrate that the differences in the ADC time series data between the ctl and GLT1-KD mice reflect differences in tissue function rather than tissue microstructure, we examined the magnitude of the $ADC_{baseline}$ as well as the frequency of the "ADC-driving events" (See the IDMI analysis for a definition of "driving events" in the Methods), and the amplitude of the ADC fluctuation (Fig. 2A). The frequency of the ADC-driving events in the CST circuitry of GLT1-KD mice was higher than that of ctl mice (Fig. 2D, E and Table S2). To compare the synchronization of the ADC-driving events, we examined the peristimulus time histograms (PSTHs) of the ADC-driving events in the CST circuitry and found that events in the GLT1-KD mice were more synchronized than those of the ctl mice (Fig. 2F). Next, we calculated the power spectrum of the ADC time-series data to compare the amplitude of the ADC fluctuation. The GLT1-KD mice showed increased spectrum power in the CST circuitry compared to ctl mice (Fig. 2G and Table S3). In addition, the magnitude of the $ADC_{baseline}$ and the frequency of the ADC-driving events were significantly correlated with the generation of tic-like behavior (Table S4) and with GLT1 expression levels (Table S4). In comparison, there were no significant differences in the frequency or amplitude based on the BOLD-fMRI (Figure S3B-E). The S_{b1000} and S_{b1800} signals also showed no significant change in the ORB (Figure S6A). Together, these results indicate that the GLT1-KD mice exhibited hyperactivation of the CST circuitry, and this hyperactivation was associated with tic-like behavior.

3.3. *FC patterns derived from S_{b1800}-DfMRI signals*

Our previous study using pharmacological DfMRI reported that the direct localized infusion of cell swelling modulators induced changes in DfMRI signals in remote regions of the cortex, which were functionally connected with those local regions, suggestive of cellular swelling-related connectivity (Abe et al., 2017a). From this evidence, relying on a previous DfMRI study which revealed functional connectivity between pharmacologically challenged thalamic nuclei and remote cortical regions, we hypothesized that FC could be analyzed using DfMRI signals, similar to FC analyses performed with resting state BOLD-fMRI. We calculated the FC as a pairwise Pearson's correlation of the time series from S_{b1800} between brain nodes, then generated FC maps with the seeded bilateral ROIs of 59 brain loci (Fig. 3A). We compared the FC patterns derived from S_{b1800}-DfMRI or BOLD-fMRI to examine the similarity between the DfMRI-based connectivity and the pre-determined connectivity defined by BOLD-fMRI. In particular, positive correlations in the FC maps with seeded ROIs related to CST circuitry and in the connectivity matrix over the 59 brain loci showed similar localization patterns of the FCs between the S_{b1800}-DfMRI and BOLD-fMRI signals (Fig. 3A, B). These connectivity patterns were significantly correlated (r=0.74,

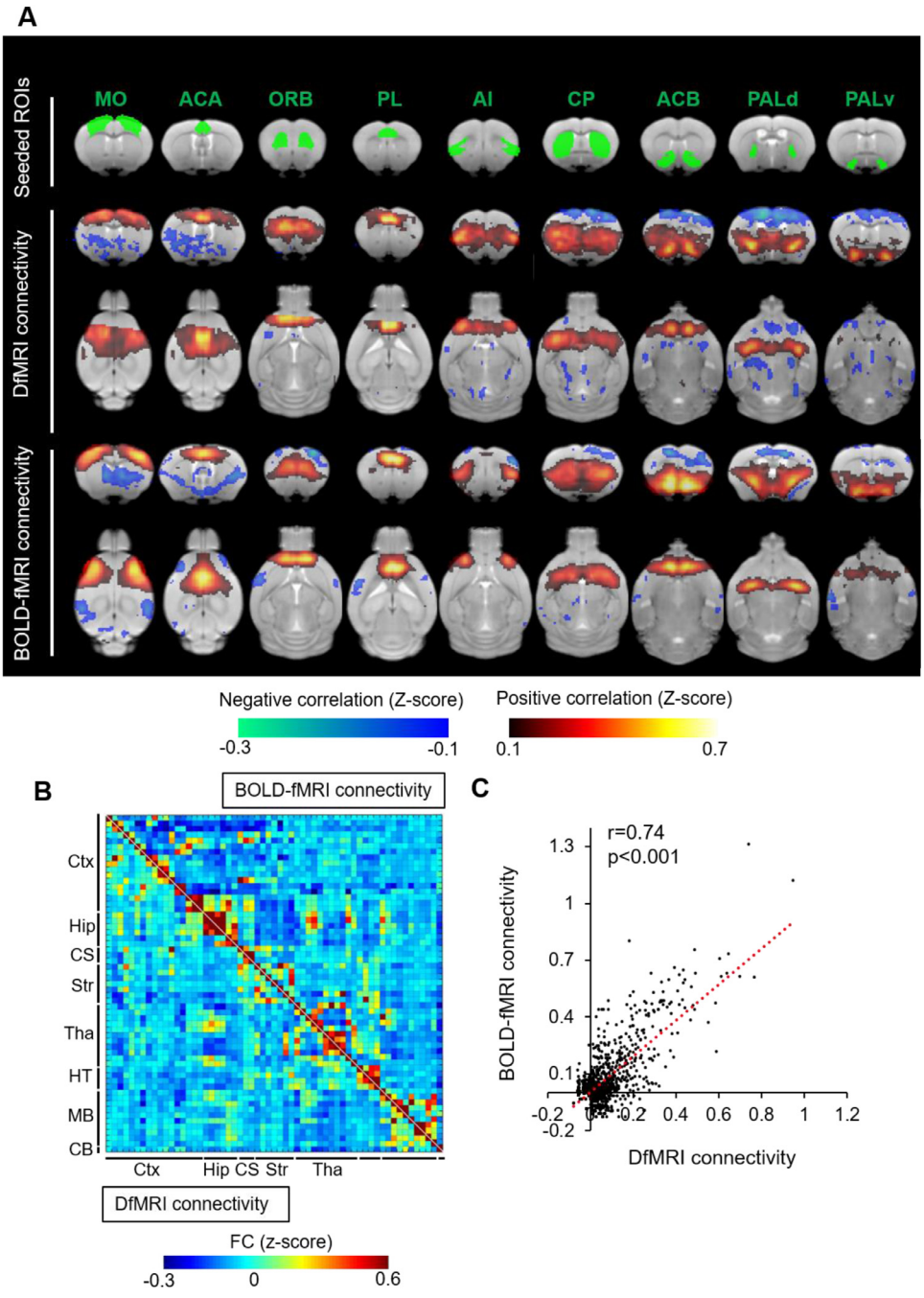

Fig. 3. FC pattern derived by S_{b1800}-DfMRI in control mice. (A) Representative averaged FC maps were compared between S_{b1800}-DfMRI (middle panels) and BOLD-fMRI (lower panels). The green regions (upper panels) show the seeded ROIs of 9 regions. All connectivity was calculated using only ctl mice (n=14). (B) FC matrices for each point of connectivity throughout the whole brain (isocortex: Ctx; hippocampus: Hip; cortical subplate: CS; striatum: Str; thalamus: Tha; hypothalamus: HT; midbrain: MB; and cerebellum: CB) are shown in the lower (DfMRI connectivity) and upper (BOLD-fMRI connectivity) halves. The color bar represents the FC z-score. (C) Plots of the FCs between the BOLD-fMRI and the S_{b1800}-DfMRI. The black dots are the FCs of the DfMRI and BOLD-fMRI for each pathway of the combinations from the 59 × 59 FC matrix (1711 pathways).

p<0.001; Fig. 3C). Positive FC maps using seeded ROIs from the DfMRI also identified the same connectivity pattern as previously determined from the BOLD-fMRI (Sforazzini et al., 2014; Zerbi et al., 2015). In contrast, the negative correlation with DfMRI exhibited less functional localization of the connectivity than with the BOLD-fMRI (Fig. 3A, B). Overall, these results support the assumption that DfMRI-S_{b1800} signals can be used for FC analysis. However, the connectivity patterns derived from DfMRI were not identical to those from BOLD-fMRI, likely due to the confounding hemodynamic effects associated with BOLD-fMRI.

3.4. GLT1-KD mice have FC abnormalities in the CST circuitry

We compared the FCs derived from the S_{b1800} between the ctl and GLT1-KD mice (Fig. 4A). FC analysis was focused on the CST circuitry based on ADC-DfMRI results. We found significant differences in FC between ctl and GLT1-KD mice (Fig. 4B, C). The positive FCs were enhanced in the pathways that included the MO-ILA, MO-ORB, SS-ORB, and the SS-CP, and were reduced in the pathways that included the OBF-VIS, ORB-ACB, and the PALd-MED. In contrast, the negative FCs were enhanced in the ILA-PALd pathway, and were reduced in the pathways that included the MO-PALd, MO-MED, SS-PALv, VIS-SNr, ACA-PALv, PL-PALd, and the RSP-PALd. In addition, tic-like behavior was positively correlated with the FC of the MO-ILA, MO-ORB, MO-MED, ACA-PALv, PL-PALd, PL-VENT, ORB-RSB, RSB-MED, AI-VENT, ACB-PALv, and the ACB-MED, and negatively correlated with the FC of the SS-VIS, VIS-ACA, ACA-AI, ORB-ACB, and the RSB-ACB (Fig. 4D). These FC changes of the pathway were also significantly correlated with GLT1 expression levels (Table S5).

We compared the FCs in the hippocampal network to assess the specificity of the FC differences in the CST circuitry. Brain regions were chosen in the hippocampus (DG, CA3, CA1, subiculum), the associated cortex (MO, SS, ACA, PL, ILA, and RSB), the entorhinal cortex (ENT),

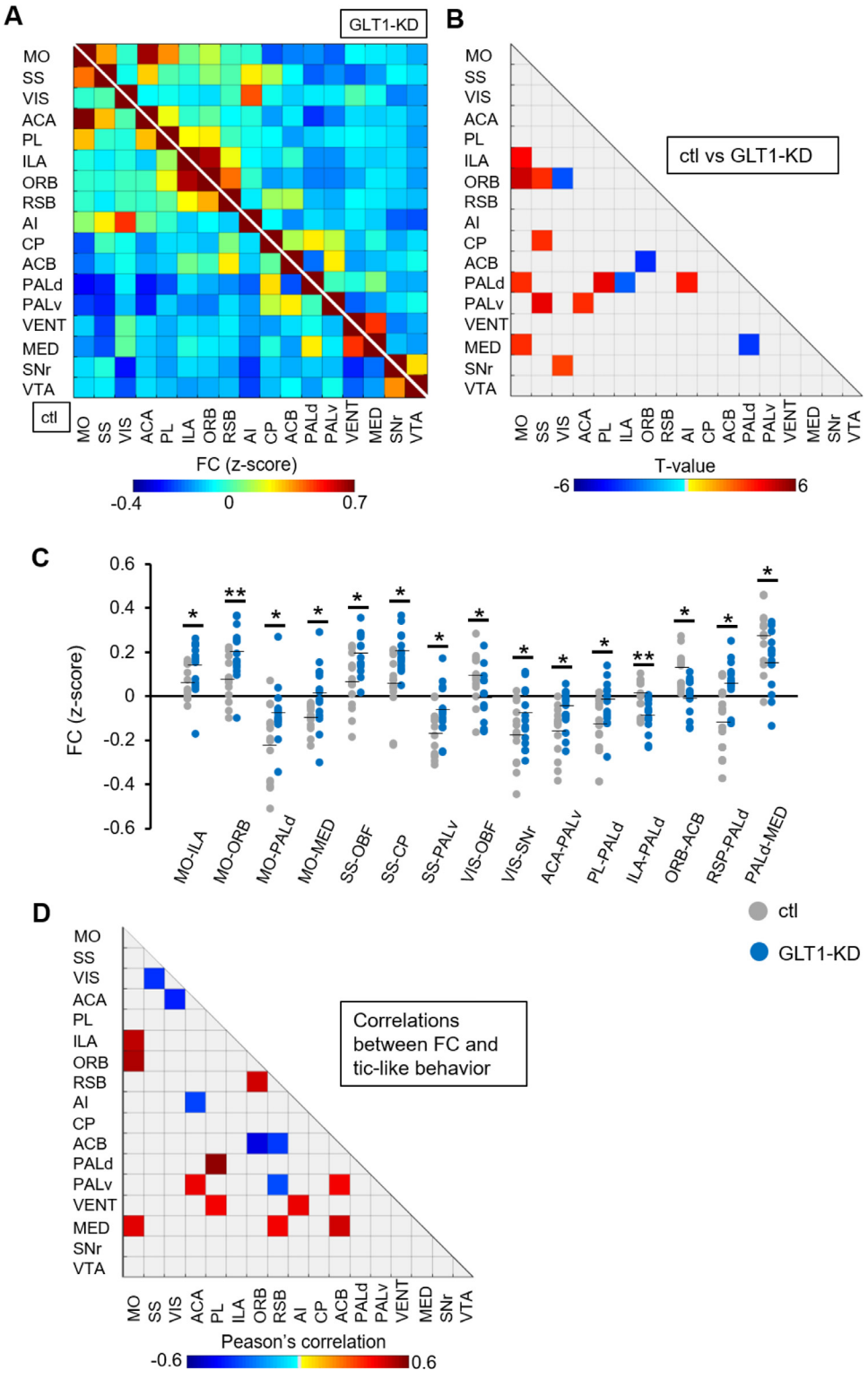

Fig. 4. FC analysis found biased connectivity across the CST circuitry in GLT1-KD mice. (A) The FC matrix for each connectivity point across the CST circuitry is shown in the lower (ctl, n=14) and the upper (GLT1-KD, n=14) halves. The color bar represents the FC z-score. (B) The matrix shows significant differences in the FC values of the CST circuitry between ctl and GLT1-KD mice (FDR corrected $p<0.05$). The red/yellow areas represent increased FCs in GLT1-KD mice while the blue areas represent decreased FC. The gray areas represent no significant change. (C) Comparisons of the FC z-scores of specific pathways, obtained from Fig. 4B, between ctl and GLT1-KD mice. * $p<0.05$, ** $p<0.01$ (FDR-corrected p-value from a two-sided t-test: ctl vs. GLT1-KD). The horizontal lines represent the mean. (D) Pearson's correlations between the FCs of each pathway and tic-like behavior in the ctl and KD mice are shown. The red/yellow areas represent a significant positive correlation while the blue color represents a significant negative correlation (FDR corrected $p<0.05$). Gray areas represent no significant correlation.

the amygdala (BLA), and the septum (LSX). We found no significant differences in the FCs between the ctl and GLT1-KD mice (Figure S7C, D). In addition, when we compared the FCs calculated from the S_{b1000} and S_{b1800} to evaluate the FC differences between the ctl and GLT1-KD mice, we found that the FC derived from the S_{b1000} in the pathway of the MO-MED was increased in the GLT1-KD mice and the FC of the CP-ACB was decreased (Figure S7A, B). However, the FC differences in the S_{b1000} were less than those in the S_{b1800}, indicating that the S_{b1800} is better to evaluate the FC.

Together, these results indicate that GLT1-KD mice have FC abnormalities in CST circuitry, and this connectivity impairment is associated with the generation of tic-like behavior.

3.5. IDMI analysis reveals abnormal propagation of local activity to the global network

To elucidate the relationship between hyperactivation and abnormal FC patterns, we performed an ignition-driven mean integration (IDMI)

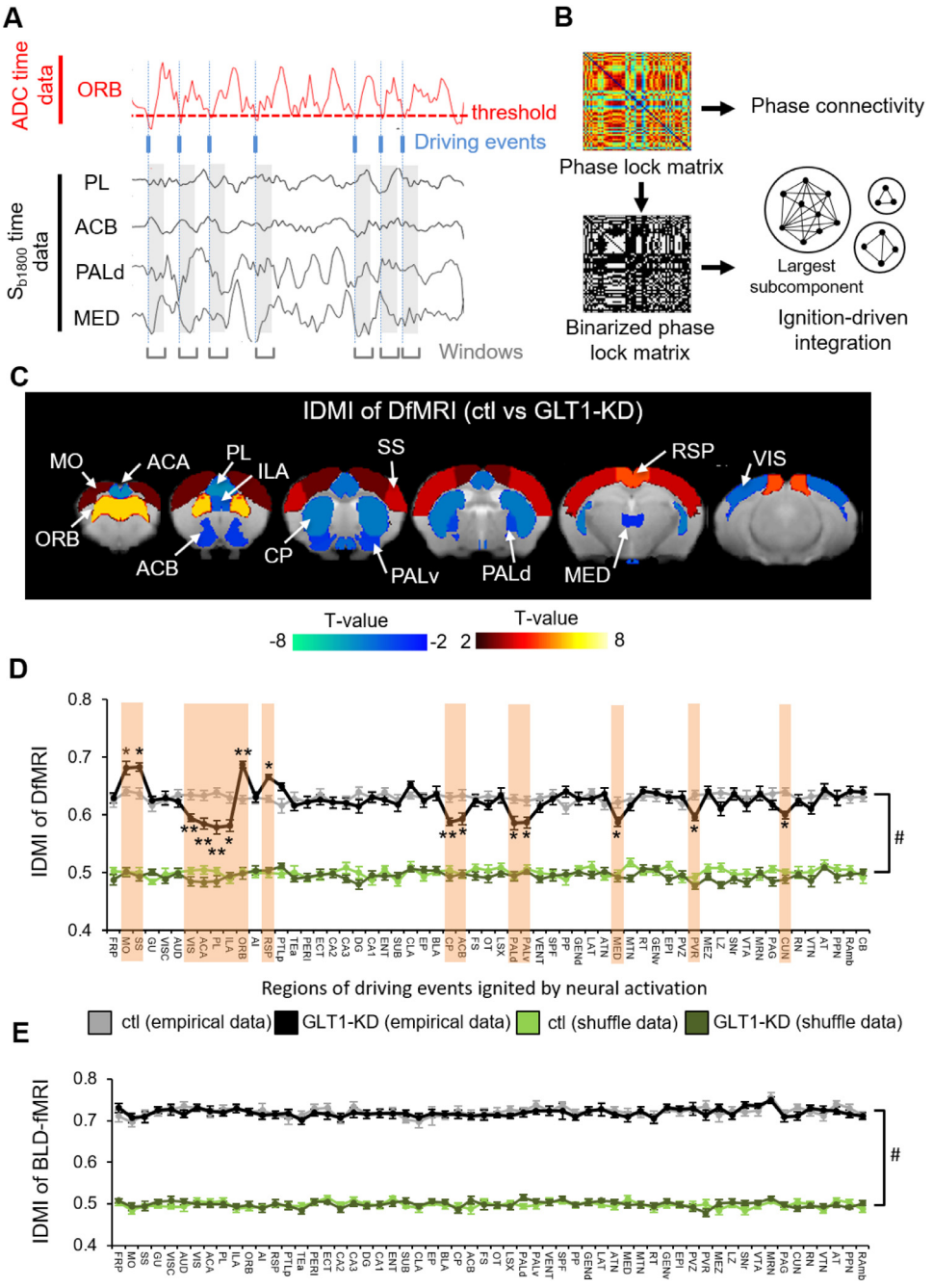

Fig. 5. The IDMI analysis with DfMRI data reveals alterations in local activity-initiated propagation across the CST circuitry. (A) A flowchart of the IDMI analysis for a given brain region using the ORB (red) as an example to estimate the driving event. The IDMI value reflects the amount of neural propagation from a given brain region to the global network. The time points (ADC driving events: single blue bar), reflecting neural excitation coupled with decreases in ADC, were estimated from the ADC time-series data (red line) corresponding to a given threshold. The black lines show the time-series data from S_{b1800} in the PL, ACB, PALd, and MED. (B) A phase lock matrix was computed by averaging over each time window (gray areas in Fig. 5A) of the time-series data from S_{b1800}. We identified phase connectivity differences by comparing the phase lock matrix. From the binarized matrix of the phase lock matrix, the ignition-driven integration was calculated by identifying the largest subcomponent and averaging over the time windows. (C) Brain ROIs showing significant DfMRI-IDMI changes (FDR corrected $p<0.05$) were plotted: n=14 in ctl and n=14 in GLT1-KD mice. The red/yellow areas represent an increase in IDMI in GLT1-KD mice, while the blue areas represent the opposite. (D) The IDMI derived from the DfMRI of each driving event was compared between the ctl (gray) and GLT1-KD (black) mice (two-way repeated-measures ANOVA, main effect of genotype $F_{1,1534}=9.12$, $p=2.57\times10^{-3}$, interaction effect $F_{58,1534}=1.36$, $p=0.041$). * $p<0.05$, ** $p<0.01$ (FDR corrected p-value from a two-sided t-test: ctl vs. GLT1-KD). The IDMI by the green line was calculated from the shuffled time-series data from S_{b1800} to validate the IDMI values derived from empirical data. # $p<0.001$ (repeated two-way ANOVA to compare empirical and shuffle data in ctl, the main effect of data type $F_{1,1534}=2687.62$, $p<1.0\times10^{-23}$, interaction effect $F_{58,1534}=0.45$, $p=0.99$). (E) The IDMI derived from the BOLD-fMRI did not significantly change between the ctl (n=14) and GLT1-KD mice (n=14) (two-way repeated-measures ANOVA, main effect of genotype $F_{1,1534}=0.17$, $p=0.68$, interaction effect $F_{58,1534}=0.81$, $p=0.85$). Polygonal lines represent the mean and vertical lines represent the standard error (s.e.m.).

analysis. IDMI analysis has been proposed to examine how intrinsic local activation is propagated into whole brain regions (Deco and Kringelbach, 2017; Deco et al., 2017). However, the correct events of intrinsic local activation, which was defined by increases in the BOLD signal may not be detected because of hemodynamic confounding effects (Figure S3). In the current study, the events of intrinsic local activation were defined based on reductions in the ADC values. The IDMI values were then calculated from the event-related phase synchronized connectivity of the S_{b1800} data (Fig. 5A, B).

Before comparing the IDMI values between the ctl and GLT1-KD mice, we determined the best band path filter range to evaluate differences in the IDMI values. We compared the IDMI values obtained using several filters with a narrow range (0.01-0.04, 0.02-0.05, 0.03-0.06, 0.04-0.07, 0.05-0.08, 0.06-0.09, 0.07-0.1 Hz) and one with a broad range (0.01-0.1 Hz) (Figure S4B, C). With the DfMRI, the IDMI values of the empirical data were not distinguishable from those of the shuffled data with filters of the lower narrow ranges (0.01-0.04, 0.02-0.05, 0.03-0.06 Hz) and the broad range (0.01-0.1 Hz). In contrast, empirical data were distinguished from shuffled data with the filters of higher ranges (0.04-0.07, 0.05-0.08, 0.06-0.09, 0.07-0.1). With the filter range of 0.05-0.08 Hz, we were able to see many differences in the IDMI values of the empirical data between the ctl and GLT1-KD mice. In the BOLD-fMRI, the IDMI values showed the same behavior as in the DfMRI. The BOLD-IDMI values for the filter range of 0.04-0.07 Hz showed the largest difference between the empirical and shuffled data, in agreement with a previous study (Deco et al., 2017). Hence, in this study, we applied the same narrow filter of 0.05-0.08 Hz to the IDMI analysis with both the BOLD-fMRI and DfMRI to facilitate the comparison. Next, we investigated which of the diffusion signals among the S_{b1000}, S_{b1800}, and ADC best distinguished the ctl and GLT1-KD mice with the IDMI values

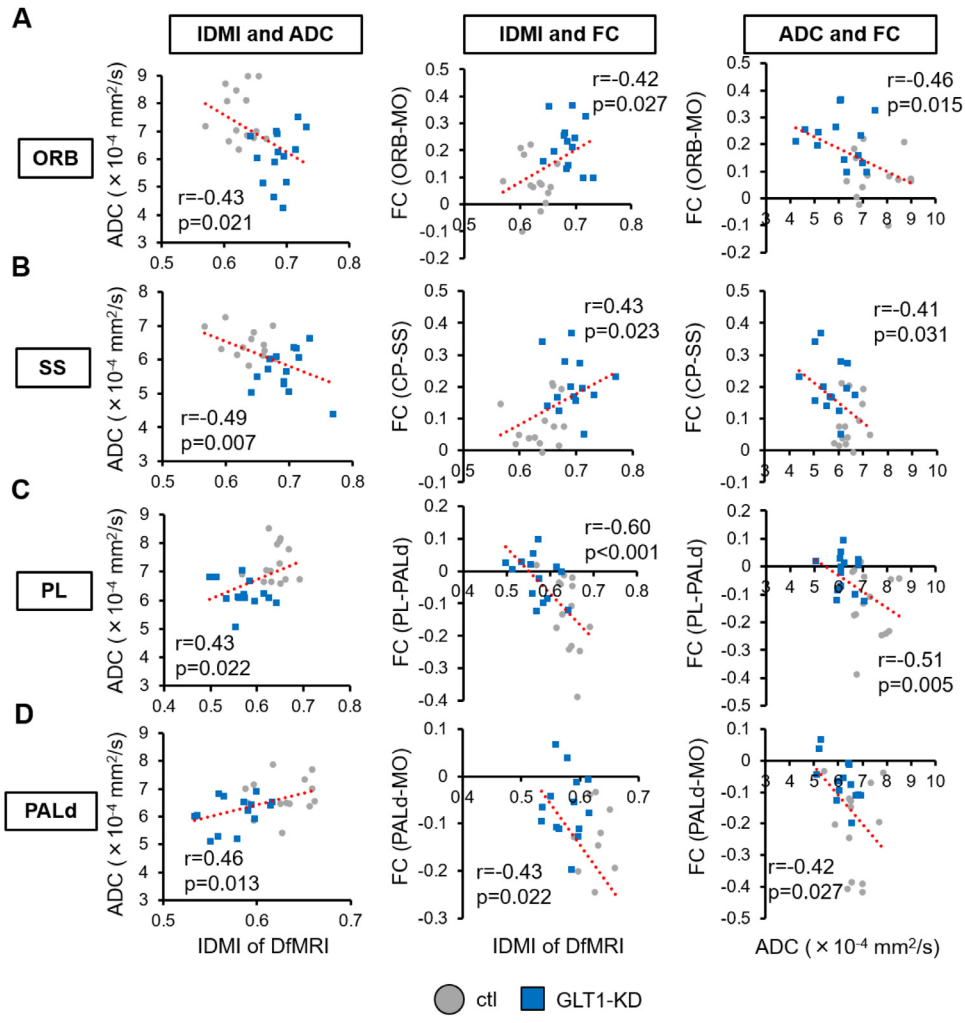

Fig. 6. Local activity-initiated propagation is associated with resting state activity and functional connectivity. (A-D) Correlations between IDMI and ADC (left panels), IDMI and FC of a given pathway (middle panels), and ADC and FC (right panels) for the ORB (A), SS (B), CP (C), and PALd (D). The ORB and SS show increased information propagation that is correlated to increased resting state activity detected by ADC and enhanced connectivity. In contrast, the CP and PALd show that decreases in information propagation are correlated with increases in resting state activity and weakened connectivity.

(Figure S6). The best results were obtained from the IDMI values when we used the ADC to define the intrinsic driving events and the S_{b1800} to calculate the phase connectivity (Fig. 5D versus Figure S6B-E). Together, we calculated the IDMI values using the ADC and S_{b1800} filtered by 0.05-0.08 Hz.

When we compared the IDMI values between the ctl and GLT1-KD mice, we found that the IDMI value was increased in the MO, SS, ORB, and RSP, and decreased in the VIS, ACA, PL, ILA, CP, ACB, PALd, PALv, MED, PVR, and CUN in GLT1-KD mice (Fig. 5C, D). The increase in the IDMI reflected an increase in neural propagation from the intrinsic local activation initiated by a given brain region to the global network, while the decrease in the IDMI reflected a decrease in neural propagation. These IDMI changes were positively or negatively correlated with the generation of tic-like behavior (Table S4). They were also correlated with GLT1 expression levels (Table S4). In contrast, there were no significant changes in the IDMI values calculated from the BOLD-fMRI signals (Fig. 5E).

Next, we investigated the relationship between the IDMI values and the ADC or FC. In the ORB, SS, MO, and RSP, which had increased IDMI, the decrease in ADC (hyperactivation) was related to the increase in IDMI and enhancement of connectivity (Fig. 6A, B, and Figure S8). In contrast, in the PL, PALd, and MED, which had the decreased IDMI, the decrease in the ADC was related to the decrease in the IDMI and a weakening of the connectivity (Fig. 6C, D, and Figure S8). These results indicate that hyperactivation of the CST circuitry was associated with abnormal connectivity and neural propagation. However, these relationships did not apply to all brain regions with observed changes in the IDMI, such as the CP, ACB, and PALv (Figure S8).

Lastly, we examined which propagation pathway in the CST circuitry was affected by hyperactivation. We calculated local activity-initiated phase-synchronized connectivity in the brain regions with significant IDMI changes. The phase connectivity initiated from the ORB, MO, and SS, which had increased IDMI, was increased in GLT1-KD mice (Figure S9A-C). In contrast, the phase connectivity initiated from the PL, ILA, CP, ACB, PALd, PALv, and MED, which had decreased IDMI values, was decreased in the GLT1-KD mice (Figure S9D-J). This indicates that the IDMI alterations in the CST circuitry were associated with abnormal connectivity. When we investigated the phase-synchronized connectivity with the BOLD-fMRI, there were a few pathways with increased phase connectivity, such as the ORB-SNr, PL-ACA, ACB-PALd, MED-ORB, and MED-PL (Figure S10). Together, these results indicate that the GLT1-KD mice exhibited an unbalanced distribution of neural propagation in the CST circuitry, and this abnormal propagation was associated with tic-like behavior.

4. Discussion

Astrocytes have an important role in the modulation of neurovascular coupling, the mechanism underlying BOLD-fMRI (Schulz et al., 2012). GLT1 is a major glial glutamate transporter in the forebrain (Tanaka et al., 1997). In GLT1-KD mice ($GLAST^{CreERT2/+}$; $GLT1^{flox/flox}$), the expression of not only GLT1, but also GLAST, another major glial

glutamate transporter, is likely decreased. A previous BOLD-fMRI study using optogenetics found that astrocytes could generate BOLD-fMRI responses without neuronal modulation (Takata et al., 2018). Hence, astrocyte dysfunction might lead to abnormal hemodynamic responses, as likely occurs in GLT1-KD mice (Murphy-Royal et al., 2017; Robinson and Jackson, 2016).

A decrease in the magnitude of the ADC baseline was detected by DfMRI, as well as increases in the ADC driving events and the amplitude of the ADC fluctuation in the CST circuitry of GLT1-KD mice, indicating hyperactivation. The hyperactivation was likely induced by an increase in the extracellular glutamate concentration due to knock down of the glutamate transporters (GLT1 as well as GLAST). A previous electrophysiological study using the same GLT1-KD strain showed an increase in seizure severity introduced by kainic acid and an enhancement of the evoked excitatory postsynaptic potential (EPSP) amplitude in the striatum (Aida et al., 2015). Consistently, habenula-specific GLT1-KD mice showed neural excitation in the habenula (Cui et al., 2014). In other animal models of repetitive behaviors (tic and grooming), enhanced activity in striatal circuitry was observed in mice with Sappa3 (a postsynaptic scaffolding protein gene) knockdown (Ade et al., 2016), and enhanced synaptic excitability in the striatum and amygdala was observed in SPRED2 (a protein expressed in various brain regions and a potent inhibitor of Ras/ERK-MAPK signaling) knockdown mice (Ullrich et al., 2018). In addition, optogenetic excitation of the ORB neuron terminals at the ACB induced an increase in grooming behavior (Ahmari et al., 2013). In clinical studies, the amplitude of low frequency fluctuations (ALFF) analysis of BOLD-fMRI with OCD patients suggested hyperactivation in the striatum, ORB, and ACA (Hou et al., 2012; Yang et al., 2019). However, results from the ALFF analysis of BOLD-fMRI should be interpreted with caution due to confounding hemodynamic effects. In fact, when we compared by power spectrum analysis, the amplitude of the time-series data from the BOLD and diffusion signals (S_{b1000} and S_{b1800}), which still retained residual vascular effects, there were no significant differences between the ctl and GLT1-KD mice (Figure S3 and Figure S6A). Collectively, these reports support our ADC-DfMRI findings that GLT1-KD mice exhibit hyperactivation of the CST circuitry. Furthermore, our results show that local resting state activity can be evaluated using ADC-fMRI.

In the FC analysis, the spatial patterns of the positive correlation in the FC derived from the S_{b1800}-DfMRI showed similar localization to those from the BOLD-fMRI (Sforazzini et al., 2014; Zerbi et al., 2015). In particular, the spatial pattern of the positive correlations of the FC from the DfMRI coincided with the spatial patterns of the neural activity observed by calcium imaging of the brain surface (Ma et al., 2016; Wright et al., 2017). In contrast, the spatial patterns of the negative correlations in the DfMRI FC did not coincide with those from the BOLD-fMRI. Indeed, the link between the negative BOLD signals with the actual activity decrease remains controversial. One likely explanation for the discrepancy between the DfMRI FC and BOLD-fMRI FC is the effect of the blood vessel distribution, to which the BOLD-fMRI is sensitive by principle, while the DfMRI is not (Abe et al., 2017a; Tsurugizawa et al., 2013). Moreover, those discrepancies might result from differences in the intrinsic time course of the temporal responses for the DfMRI and BOLD-fMRI signals. The DfMRI signals have been shown to be faster than the BOLD-fMRI signals (Aso et al., 2013; Aso et al., 2009; Le Bihan et al., 2006; Nunes et al., 2019). Further investigation is needed to clarify the nature of the negative FC correlation found with the DfMRI and BOLD fMRI.

Using DfMRI FC analysis, we detected enhanced or weakened connectivity of some pathways in the CST circuitry of GLT1-KD mice. Our DfMRI FC results obtained with this mouse model somewhat differed from previous FC results obtained with BOLD-fMRI in OCD patients. Some groups have shown an FC increase in the ORB-striatal pathway as well as in the striato-thalamic pathway (Abe et al., 2015; Hou et al., 2014), while another group reported a decrease in the FC in the ORB-striatal pathway(Jung et al., 2017). These reports suggest that OCD patients may have FC impairments in CST circuitry, in agreement with our DfMRI FC results.

In the IDMI analysis of the DfMRI, we found an unbalanced distribution of neural propagation initiated by local activity to the global network in the GLT1-KD mice. This result not only confirms abnormal dynamic brain function related to CST circuitry, but also links hyperactivation of the CST circuitry with bidirectional alterations in local activity-initiated propagation. In addition, the analysis of the local activity-initiated phase-synchronized connectivity provided us with information on the directional pathways, which displayed altered propagation. According to previous reports, higher IDMI variability implied a hierarchical function across brain regions (Deco and Kringelbach, 2017; Deco et al., 2017). We observed an increase in the variability of the DfMRI-IDMI values in the GLT1-KD mice compared to controls (Figure S11), indicating that the GLT1-KD mice exhibited more hierarchical brain organization. In contrast, the IDMI analysis using the BOLD-fMRI detected less alteration in the GLT1-KD mice than found using the DfMRI. Additionally, there were no differences in frequency synchronization of the BOLD-fMRI driving events, amplitude of the fluctuations (Figure S3), or the AUC (See the methods) between the ctl and GLT1-KD mice (Figure S4D). Overall, these differences highlight the various mechanisms underlying the DfMRI and BOLD-fMRI and, for the BOLD-fMRI, a high sensitivity to neurovascular coupling perturbations may result from astroglial dysfunction. DfMRI clearly has an advantage in reflecting dynamic brain function without interference from confounding hemodynamic effects.

The difference between BOLD and DfMRI responses is epitomized when using the ADC rather than the raw S_{b1800} and S_{b1000} signals, also indicating that vascular effects (on which BOLD-fMRI is fully based) are present, although to a much lesser degree, in the raw DfMRI signal, but eliminated when using the ADC (Abe et al., 2017a; Aso et al., 2009; Komaki et al., 2020; Le Bihan et al., 2006; Nunes et al., 2019; Tsurugizawa et al., 2013). While the exact mechanisms underlying the DfMRI signal responses remain to be fully elucidated the different patterns we observed between DfMRI and BOLD fMRI clearly support the hypothesis that the link of DfMRI and BOLD fMRI responses with neural activation rely on different mechanisms and have a different origin, as also reported by other groups (Albers et al., 2019). Pharmacological studies (Abe et al., 2017a) and MRI microscopy studies (Abe et al., 2017b) have suggested that neural swelling could be a putative mechanism of DfMRI, but this hypothesis remains to be validated, which was out of the scope of this study.

The dependence of the results (ADC, FC, and IDMI) on the b values (Figures S6 and S7A, B) might appear as a limitation. Indeed, it has been shown that the relative contribution of the genuine diffusion effects increases with higher b-values, while the amount of residual vascular effects remains the same at all b-values (Aso et al., 2009). The relative amplitude of the ADC change is expected to be larger when using high b values because non-Gaussian diffusion is more sensitive to tissue microstructure and physiology (Le Bihan and Iima, 2015). The issue is then that the signal attenuation from diffusion becomes large, which decreases the overall SNR and the degree of statistical significance of the observed changes. Indeed, S_{b1000} and S_{b1800} were noisier than the BOLD images (Figure S1B). Nonetheless, we could obtain significant differences in DfMRI studies between the ctl and GLT1-KD mice. This SNR issue is perhaps the most important limitation of DfMRI compared to BOLD fMRI, but it is expected that this limitation would be overcome in the future with the availability of MRI systems equipped with strong gradient hardware. Another limitation is that the somewhat narrow filtering (0.05-0.08 Hz) to calculate the IDMI value may have erased features regarding the specificity of the DfMRI and BOLD-fMR, although, we were careful to validate the proper filtering range to best detect functional differences between the ctl and GKT1-KD mice (Figure S4B, C).

5. Conclusion

We found abnormalities of dynamic brain function in neuropsychiatric conditions by leveraging the advantages of DfMRI. The ability to obtain hemodynamic-independent measurements by DfMRI is a strong advantage for the detection of local activity-initiated propagation to the global network in neuropsychiatric conditions, which may be poorly visualized with BOLD-fMRI due to confounding vascular effects. The implications of our DfMRI approaches are important not only for clinical DfMRI studies in healthy subjects (Aso et al., 2013; Le Bihan et al., 2006; Miller et al., 2007; Nicolas et al., 2017; Williams et al., 2014; Williams et al., 2016) but are even more critical when performing BOLD-fMRI in geriatric patients with common comorbid vascular response dysfunctions.

Declaration of Competing Interest

The authors report no biomedical financial interests or potential conflicts of interest.

CRediT authorship contribution statement

Yoshifumi Abe: Conceptualization, Methodology, Software, Validation, Formal analysis, Investigation, Writing - original draft, Visualization, Funding acquisition, Project administration. **Norio Takata:** Methodology, Software, Funding acquisition. **Yuki Sakai:** Methodology, Software. **Hiro Taiyo Hamada:** Investigation, Resources. **Yuichi Hiraoka:** Resources. **Tomomi Aida:** Resources, Funding acquisition. **Kohichi Tanaka:** Resources, Funding acquisition. **Denis Le Bihan:** Writing - review & editing. **Kenji Doya:** Supervision, Funding acquisition. **Kenji F Tanaka:** Supervision, Funding acquisition, Project administration, Writing - review & editing.

Acknowledgments

We thank Jiafu Zeng for animal support during the acclimation of the mice for MRI acquisition.

Funding

This work was supported by a Grant-in-Aid for Research Fellowships of the Japan Society for the Promotion of Science (JSPS Research Fellow) under grant number 18J00922 (Y.A.), Early-Career Scientists of JSPS KAKENHI under grant number 19K16298 (Y.A.), Grant-in-Aid for Scientific Research (C) under grant number 16K07032 (N.T.), Grant-in-Aid for Scientific Research on Innovative Areas under grant number 18H04952 (N.T.), the joint Usage/Research Program from MRI of TMDU (K.T., T.A., K.F.T.), Takeda Science Foundation (Y.A., T.A.), and research support of Okinawa Institute of Science and Technology Graduate University for the Neural Computation Unit (K.D.).

Supplementary materials

Supplementary material associated with this article can be found, in the online version, at doi:10.1016/j.neuroimage.2020.117318.

References

Abe, Y., Sakai, Y., Nishida, S., Nakamae, T., Yamada, K., Fukui, K., Narumoto, J., 2015. Hyper-influence of the orbitofrontal cortex over the ventral striatum in obsessive–compulsive disorder. Eur. Neuropsychopharmacol. 25, 1898–1905.

Abe, Y., Tsurugizawa, T., Le Bihan, D., 2017a. Water diffusion closely reveals neural activity status in rat brain loci affected by anesthesia. PLoS Biol. 15, e2001494.

Abe, Y., Van Nguyen, K., Tsurugizawa, T., Ciobanu, L., Le Bihan, D., 2017b. Modulation of water diffusion by activation-induced neural cell swelling in Aplysia Californica. Sci. Rep. 7, 6178.

Ade, K.K., Wan, Y., Hamann, H.C., O'Hare, J.K., Guo, W., Quian, A., Kumar, S., Bhagat, S., Rodriguiz, R.M., Wetsel, W.C., Conn, P.J., Dzirasa, K., Huber, K.M., Calakos, N., 2016. Increased metabotropic glutamate receptor 5 signaling underlies obsessive-compulsive disorder-like behavioral and striatal circuit abnormalities in mice. Biol. Psychiatry 80, 522–533.

Ahmari, S.E., Spellman, T., Douglass, N.L., Kheirbek, M.A., Simpson, H.B., Deisseroth, K., Gordon, J.A., Hen, R., 2013. Repeated cortico-striatal stimulation generates persistent OCD-like behavior. Science 340, 1234–1239.

Aida, T., Yoshida, J., Nomura, M., Tanimura, A., Iino, Y., Soma, M., Bai, N., Ito, Y., Cui, W., Aizawa, H., Yanagisawa, M., Nagai, T., Takata, N., Tanaka, K.F., Takayanagi, R., Kano, M., Gotz, M., Hirase, H., Tanaka, K., 2015. Astroglial glutamate transporter deficiency increases synaptic excitability and leads to pathological repetitive behaviors in mice. Neuropsychopharmacology 40, 1569–1579.

Albers, F., Wachsmuth, L., Schache, D., Lambers, H., Faber, C., 2019. Functional MRI readouts from BOLD and diffusion measurements differentially respond to optogenetic activation and tissue heating. Front. Neurosci. 13, 1104.

Aso, T., Urayama, S., Fukuyama, H., Le Bihan, D., 2013. Comparison of diffusion-weighted fMRI and BOLD fMRI responses in a verbal working memory task. Neuroimage 67, 25–32.

Aso, T., Urayama, S., Poupon, C., Sawamoto, N., Fukuyama, H., Le Bihan, D., 2009. An intrinsic diffusion response function for analyzing diffusion functional MRI time series. Neuroimage 47, 1487–1495.

Bai, R., Stewart, C.V., Plenz, D., Basser, P.J., 2016. Assessing the sensitivity of diffusion MRI to detect neuronal activity directly. Proc. Natl. Acad. Sci. U S A 113, E1728–E1737.

Bronfeld, M., Bar-Gad, I., 2013. Tic disorders: what happens in the basal ganglia? Neuroscientist 19, 101–108.

Cerliani, L., Mennes, M., Thomas, R.M., Di Martino, A., Thioux, M., Keysers, C., 2015. Increased functional connectivity between subcortical and cortical resting-state networks in autism spectrum disorder. JAMA Psychiatry 72, 767–777.

Cotero, V., Fan, Y., Tsaava, T., Kressel, A.M., Hancu, I., Fitzgerald, P., Wallace, K., Kaanumalle, S., Graf, J., Rigby, W., Kao, T.J., Roberts, J., Bhushan, C., Joel, S., Coleman, T.R., Zanos, S., Tracey, K.J., Ashe, J., Chavan, S.S., Puleo, C., 2019. Noninvasive sub-organ ultrasound stimulation for targeted neuromodulation. Nat. Commun. 10, 952.

Cui, W., Mizukami, H., Yanagisawa, M., Aida, T., Nomura, M., Isomura, Y., Takayanagi, R., Ozawa, K., Tanaka, K., Aizawa, H., 2014. Glial dysfunction in the mouse habenula causes depressive-like behaviors and sleep disturbance. J. Neurosci. 34, 16273–16285.

Deco, G., Kringelbach, M.L., 2017. Hierarchy of information processing in the brain: a novel 'Intrinsic Ignition' framework. Neuron 94, 961–968.

Deco, G., Tagliazucchi, E., Laufs, H., Sanjuan, A., Kringelbach, M.L., 2017. Novel intrinsic ignition method measuring local-global integration characterizes wakefulness and deep sleep. eNeuro 4.

Ellegood, J., Babineau, B.A., Henkelman, R.M., Lerch, J.P., Crawley, J.N., 2013. Neuroanatomical analysis of the BTBR mouse model of autism using magnetic resonance imaging and diffusion tensor imaging. Neuroimage 70, 288–300.

Hikishima, K., Komaki, Y., Seki, F., Ohnishi, Y., Okano, H.J., Okano, H., 2017. In vivo microscopic voxel-based morphometry with a brain template to characterize strain-specific structures in the mouse brain. Sci Rep 7, 85.

Hou, J., Wu, W., Lin, Y., Wang, J., Zhou, D., Guo, J., Gu, S., He, M., Ahmed, S., Hu, J., Qu, W., Li, H., 2012. Localization of cerebral functional deficits in patients with obsessive-compulsive disorder: a resting-state fMRI study. J. Affect. Disord. 138, 313–321.

Hou, J.M., Zhao, M., Zhang, W., Song, L.H., Wu, W.J., Wang, J., Zhou, D.Q., Xie, B., He, M., Guo, J.W., Qu, W., Li, H.T., 2014. Resting-state functional connectivity abnormalities in patients with obsessive-compulsive disorder and their healthy first-degree relatives. J. Psychiatry Neurosci. 39, 304–311.

Jin, T., Kim, S.G., 2008. Functional changes of apparent diffusion coefficient during visual stimulation investigated by diffusion-weighted gradient-echo fMRI. Neuroimage 41, 801–812.

Jung, W.H., Yucel, M., Yun, J.Y., Yoon, Y.B., Cho, K.I., Parkes, L., Kim, S.N., Kwon, J.S., 2017. Altered functional network architecture in orbitofronto-striato-thalamic circuit of unmedicated patients with obsessive-compulsive disorder. Hum. Brain Mapp. 38, 109–119.

Kisler, K., Nelson, A.R., Montagne, A., Zlokovic, B.V., 2017. Cerebral blood flow regulation and neurovascular dysfunction in Alzheimer disease. Nat. Rev. Neurosci. 18, 419–434.

Komaki, Y., Debacker, C., Djemai, B., Ciobanu, L., Tsurugizawa, T., Bihan, D.L., 2020. Differential effects of aquaporin-4 channel inhibition on BOLD fMRI and diffusion fMRI responses in mouse visual cortex. PLoS One 15, e0228759.

Le Bihan, D., 2007. The 'wet mind': water and functional neuroimaging. Phys. Med. Biol. 52, R57–R90.

Le Bihan, D., Iima, M., 2015. Diffusion magnetic resonance imaging: what water tells us about biological tissues. PLoS Biol. 13, e1002203.

Le Bihan, D., Urayama, S., Aso, T., Hanakawa, T., Fukuyama, H., 2006. Direct and fast detection of neuronal activation in the human brain with diffusion MRI. Proc. Natl. Acad. Sci. U S A 103, 8263–8268.

Ma, Y., Shaik, M.A., Kozberg, M.G., Kim, S.H., Portes, J.P., Timerman, D., Hillman, E.M., 2016. Resting-state hemodynamics are spatiotemporally coupled to synchronized and symmetric neural activity in excitatory neurons. Proc. Natl. Acad. Sci. U S A 113, E8463–E8471.

Miller, K.L., Bulte, D.P., Devlin, H., Robson, M.D., Wise, R.G., Woolrich, M.W., Jezzard, P., Behrens, T.E., 2007. Evidence for a vascular contribution to diffusion FMRI at high b value. Proc. Natl. Acad. Sci. U S A 104, 20967–20972.

Montagne, A., Nation, D.A., Pa, J., Sweeney, M.D., Toga, A.W., Zlokovic, B.V., 2016. Brain imaging of neurovascular dysfunction in Alzheimer's disease. Acta Neuropathol. 131, 687–707.

Murphy-Royal, C., Dupuis, J., Groc, L., Oliet, S.H.R., 2017. Astroglial glutamate transporters in the brain: Regulating neurotransmitter homeostasis and synaptic transmission. J. Neurosci. Res. 95, 2140–2151.

Neuner, I., Werner, C.J., Arrubla, J., Stocker, T., Ehlen, C., Wegener, H.P., Schneider, F., Shah, N.J., 2014. Imaging the where and when of tic generation and resting state networks in adult Tourette patients. Front. Hum. Neurosci. 8, 362.

Nicolas, R., Gros-Dagnac, H., Aubry, F., Celsis, P., 2017. Comparison of BOLD, diffusion-weighted fMRI and ADC-fMRI for stimulation of the primary visual system with a block paradigm. Magn. Reson. Imaging 39, 123–131.

Nunes, D., Ianus, A., Shemesh, N., 2019. Layer-specific connectivity revealed by diffusion-weighted functional MRI in the rat thalamocortical pathway. Neuroimage 184, 646–657.

Power, J.D., Barnes, K.A., Snyder, A.Z., Schlaggar, B.L., Petersen, S.E., 2012. Spurious but systematic correlations in functional connectivity MRI networks arise from subject motion. Neuroimage 59, 2142–2154.

Rane, P., Cochran, D., Hodge, S.M., Haselgrove, C., Kennedy, D.N., Frazier, J.A., 2015. Connectivity in Autism: a review of MRI connectivity studies. Harv. Rev. Psychiatry 23, 223–244.

Robinson, M.B., Jackson, J.G., 2016. Astroglial glutamate transporters coordinate excitatory signaling and brain energetics. Neurochem. Int. 98, 56–71.

Schulz, K., Sydekum, E., Krueppel, R., Engelbrecht, C.J., Schlegel, F., Schroter, A., Rudin, M., Helmchen, F., 2012. Simultaneous BOLD fMRI and fiber-optic calcium recording in rat neocortex. Nat. Methods 9, 597–602.

Sforazzini, F., Schwarz, A.J., Galbusera, A., Bifone, A., Gozzi, A., 2014. Distributed BOLD and CBV-weighted resting-state networks in the mouse brain. Neuroimage 87, 403–415.

Shih, Y.Y., Chen, C.C., Shyu, B.C., Lin, Z.J., Chiang, Y.C., Jaw, F.S., Chen, Y.Y., Chang, C., 2009. A new scenario for negative functional magnetic resonance imaging signals: endogenous neurotransmission. J. Neurosci. 29, 3036–3044.

Stoodley, C.J., D'Mello, A.M., Ellegood, J., Jakkamsetti, V., Liu, P., Nebel, M.B., Gibson, J.M., Kelly, E., Meng, F., Cano, C.A., Pascual, J.M., Mostofsky, S.H., Lerch, J.P., Tsai, P.T., 2017. Altered cerebellar connectivity in autism and cerebellar-mediated rescue of autism-related behaviors in mice. Nat. Neurosci. 20, 1744–1751.

Tagliazucchi, E., Balenzuela, P., Fraiman, D., Chialvo, D.R., 2012. Criticality in large-scale brain FMRI dynamics unveiled by a novel point process analysis. Front. Physiol. 3, 15.

Takata, N., Sato, N., Komaki, Y., Okano, H., Tanaka, K.F., 2020. Flexible annotation atlas of the mouse brain: combining and dividing brain structures of the Allen Brain Atlas while maintaining anatomical hierarchy. bioRxiv 2020, 953547 02.17.

Takata, N., Sugiura, Y., Yoshida, K., Koizumi, M., Hiroshi, N., Honda, K., Yano, R., Komaki, Y., Matsui, K., Suematsu, M., Mimura, M., Okano, H., Tanaka, K.F., 2018. Optogenetic astrocyte activation evokes BOLD fMRI response with oxygen consumption without neuronal activity modulation. Glia 66, 2013–2023.

Tanaka, K., Watase, K., Manabe, T., Yamada, K., Watanabe, M., Takahashi, K., Iwama, H., Nishikawa, T., Ichihara, N., Kikuchi, T., Okuyama, S., Kawashima, N., Hori, S., Takimoto, M., Wada, K., 1997. Epilepsy and exacerbation of brain injury in mice lacking the glutamate transporter GLT-1. Science 276, 1699–1702.

Tsurugizawa, T., Ciobanu, L., Le Bihan, D., 2013. Water diffusion in brain cortex closely tracks underlying neuronal activity. Proc. Natl. Acad. Sci. U S A 110, 11636–11641.

Ullrich, M., Weber, M., Post, A.M., Popp, S., Grein, J., Zechner, M., Guerrero Gonzalez, H., Kreis, A., Schmitt, A.G., Uceyler, N., Lesch, K.P., Schuh, K., 2018. OCD–like behavior is caused by dysfunction of thalamo-amygdala circuits and upregulated TrkB/ERK-MAPK signaling as a result of SPRED2 deficiency. Mol. Psychiatry 23, 444–458.

Veldsman, M., Cumming, T., Brodtmann, A., 2015. Beyond BOLD: optimizing functional imaging in stroke populations. Hum. Brain Mapp. 36, 1620–1636.

Williams, R.J., McMahon, K.L., Hocking, J., Reutens, D.C., 2014. Comparison of block and event-related experimental designs in diffusion-weighted functional MRI. J. Magn. Reson. Imaging 40, 367–375.

Williams, R.J., Reutens, D.C., Hocking, J., 2016. Influence of BOLD contributions to diffusion fMRI activation of the visual cortex. Front. Neurosci. 10, 279.

Wright, P.W., Brier, L.M., Bauer, A.Q., Baxter, G.A., Kraft, A.W., Reisman, M.D., Bice, A.R., Snyder, A.Z., Lee, J.M., Culver, J.P., 2017. Functional connectivity structure of cortical calcium dynamics in anesthetized and awake mice. PLoS One 12, e0185759.

Yang, X., Hu, X., Tang, W., Li, B., Yang, Y., Gong, Q., Huang, X., 2019. Intrinsic brain abnormalities in drug-naive patients with obsessive-compulsive disorder: A resting-state functional MRI study. J. Affect. Disord. 245, 861–868.

Yoshida, K., Mimura, Y., Ishihara, R., Nishida, H., Komaki, Y., Minakuchi, T., Tsurugizawa, T., Mimura, M., Okano, H., Tanaka, K.F., Takata, N., 2016. Physiological effects of a habituation procedure for functional MRI in awake mice using a cryogenic radiofrequency probe. J. Neurosci. Methods 274, 38–48.

Zerbi, V., Grandjean, J., Rudin, M., Wenderoth, N., 2015. Mapping the mouse brain with rs-fMRI: An optimized pipeline for functional network identification. Neuroimage 123, 11–21.

Zhong, J., Petroff, O.A., Pleban, L.A., Gore, J.C., Prichard, J.W., 1997. Reversible, reproducible reduction of brain water apparent diffusion coefficient by cortical electroshocks. Magn. Reson. Med. 37, 1–6.